Learning by confusion: The phase diagram of the Holstein model

George Issa,[1] Owen Bradley,[1] Ehsan Khatami,[2] and Richard Scalettar[1]
[1]*Department of Physics and Astronomy, University of California, Davis, California 95616, USA*
[2]*Department of Physics and Astronomy, San José State University, San José, California 95192, USA*

(Received 14 January 2025; revised 2 April 2025; accepted 9 April 2025; published 23 April 2025)

We employ the "learning by confusion" technique, an unsupervised machine learning approach for detecting phase transitions, to analyze quantum Monte Carlo simulations of the two-dimensional Holstein model—a fundamental model for electron-phonon interactions on a lattice. Utilizing a convolutional neural network, we conduct a series of binary classification tasks to identify Holstein critical points based on the neural network's learning accuracy. We further evaluate the effectiveness of various training datasets, including snapshots of phonon fields and other measurements resolved in imaginary time, for predicting distinct phase transitions and crossovers. Our results culminate in the construction of the finite-temperature phase diagram of the Holstein model.

DOI: 10.1103/PhysRevB.111.155140

I. INTRODUCTION

Artificial intelligence (AI) and machine learning (ML) approaches have emerged as powerful techniques to study classical and quantum phase transitions (often using the output of Monte Carlo simulations as training data) [1–9], out-of-equilibrium phenomena [10–13], and also including the use of experimental data [14–19]. We refer the interested reader to recent reviews that provide comprehensive overviews of applications of AI/ML to strongly correlated models [20–22].

In the context of exploring itinerant electron Hamiltonians, one focus of ML approaches has been on the Hubbard model and understanding magnetic, charge, and exotic (d-wave) pairing correlations as well as pseudogap and strange metal phases [14,18,23–28], whereas ML investigations of electron-phonon Hamiltonians are somewhat more limited [29–32]. The Holstein model [33] has a phenomenology characterized by charge density wave (CDW) order at commensurate filling on a bipartite lattice. This insulating phase gives way to conventional (s-wave) pairing upon doping. These phases have been extensively studied with quantum simulations and conventional methods of analysis, i.e., the evaluation of order parameters and their finite-size scaling [34–44]. Several subtle effects emerge, including a nonmonotonic dependence of the superconducting transition temperature on the electron-phonon coupling strength [42,45–48], a behavior at variance with Eliashberg theory [49]. Unlike the Hubbard model, the Holstein Hamiltonian has both electronic and phonon degrees of freedom. Thus, among the questions ML methods can shed light on is which one of these degrees of freedom more clearly encodes the ordered phase.

In this paper, we apply the "learning by confusion" (LBC) method [50] to investigate the critical phenomena emerging in the half-filled Holstein model, and map out its phase diagram. At its heart, LBC consists of a series of supervised learnings with labels that change based on a guess for the location of the critical point as a tuning parameter is varied. The correct guess is expected to yield the best accuracy for the training. LBC has previously been applied to a variety of the fundamental descriptions of classical magnetic phase transitions, including the Ising [50,51] and XY [52,53] models, as well as the Blume Capel model where vacancies introduce a first-order line, which is separated by a tricritical point from the conventional second-order Ising transition [54]. Further applications of LBC include determining the critical value at which a family of quantum states become entangled [55], phase transitions between distinct steady-state behaviors in the dynamics of nonlinear polariton lattices [56], and transitions between regular and chaotic behavior in quantum billiards [57]. Topological transitions in Ising gauge theory and the toric code [58], and nonequilibrium quantum quenches captured by experimental images of ultracold atomic gases described by the one dimensional Bose-Hubbard model [11] are other recent venues where LBC has proven its utility.

Using LBC to explore electron-phonon physics offers the opportunity to study issues including (i) whether the fermionic or bosonic snapshots better encode the CDW phase and (ii) the use of space versus spacetime snapshots for the training. We also (iii) use LBC to trace a *crossover* from independent gases of up and down spin fermions in the small electron-phonon coupling region to a spatially random arrangement of empty and doubly occupied sites in the large coupling region in the absence of CDW order at relatively high temperatures. This crossover is closely analogous to that which occurs in the Hubbard model as the temperature is lowered and local moments form, but before those moments order antiferromagnetically.

The remainder of this paper is organized as follows. In Sec. II we define the Holstein Hamiltonian and discuss its physics. We also introduce the determinant quantum Monte Carlo (DQMC) method, with which we generate snapshots, and the LBC method in some detail. With this background, in Sec. III, we present results for the CDW transition and local pair crossovers in the half-filled Holstein model, and discuss the use of phonon versus electron snapshots as well as equal versus unequal time correlators. Our analysis culminates in a

phase diagram of the half-filled Holstein model in the plane of temperature and the dimensionless electron-phonon coupling. Section IV presents our concluding remarks.

II. MODEL AND METHODS

A. Holstein model

Interactions between electrons and phonons in materials give rise to dressed quasiparticles (polarons) of enhanced mass [59,60], as well as collective phenomena such as metal-insulator transitions, superconductivity, and charge-ordered states [33,37,43,61–63]. The Holstein model, given by the Hamiltonian,

$$\hat{H} = \hat{K} + \hat{U} + \hat{V}, \tag{1}$$

with

$$\hat{K} = -t \sum_{\langle ij\rangle\sigma} (\hat{c}^{\dagger}_{i\sigma}\hat{c}_{j\sigma} + \text{H.c.}) - \mu \sum_{i\sigma} \hat{n}_{i\sigma},$$

$$\hat{U} = \sum_{i} \frac{m\omega_0^2}{2}\hat{x}_i^2 + \frac{1}{2m}\hat{p}_i^2,$$

$$\hat{V} = \lambda \sum_{i\sigma} \hat{x}_i \left(\hat{n}_{i\sigma} - \frac{1}{2}\right)$$

is one of the most fundamental tight-binding models for describing electron-phonon interactions. The Hamiltonian comprises three components. The first term, $\hat{K}$, represents the nearest-neighbor electron hopping (kinetic energy) and a chemical potential μ which controls the electron density. The second term, $\hat{U}$, accounts for the dispersionless phonon kinetic and potential energy, modeled as a collection of quantum harmonic oscillators. The third term, $\hat{V}$, describes the on-site electron-phonon interaction, parametrized by the electron-phonon coupling constant λ. The electron-phonon interaction term is expressed in a particle-hole symmetric form so that half-filling $\langle \hat{n}_{i\sigma}\rangle = \frac{1}{2}$ occurs at $\mu = 0$, where also $\langle \hat{x}\rangle = 0$. We follow the usual convention of setting $m = 1$.

In this work we consider a square lattice of linear dimension L. The dispersion relation is given by $\epsilon_{\mathbf{k}} = -2t\,(\cos k_x + \cos k_y)$, with a corresponding bandwidth $W = 8t$. We introduce the dimensionless electron-phonon coupling constant $\lambda_D = \lambda^2/(\omega_0^2 W) = 2g^2/(\omega_0 W)$. Here g is the coefficient of the electron-phonon coupling when written in terms of phonon creation and destruction operators $\hat{V} = g\sum_{i\sigma}(\hat{b}_i + \hat{b}_i^{\dagger})(\hat{n}_{i\sigma} - \frac{1}{2})$.

Ignoring the phonon kinetic energy and then completing the square, one sees that the Holstein model describes an on-site phonon-mediated attractive interaction between spin up and spin down electrons given by $U_{\text{eff}} = -2g^2/\omega_0 = -\lambda^2/\omega_0^2 = \lambda_D W$. This interaction gives rise to two notable collective phenomena: (i) A finite-temperature phase transition to CDW order at half-filling and (ii) superconductivity upon doping. In the former, as temperature decreases, small bipolarons (doubly occupied sites) begin to form. Upon reaching the CDW transition temperature, these bipolarons, whose number is precisely $L \times L/2$, localize on a preferred sublattice, forming a checkerboard pattern. Two of the foci of this paper are on detecting the CDW phase transition, and showing LBC is also effective at detecting the crossover associated with the suppression of singly occupied sites (prior to CDW formation which occurs at lower temperature).

B. DQMC method

The snapshots used for training in our LBC method are generated with DQMC [64,65]. In this approach, the partition function $\mathcal{Z} = \text{Tr}\, e^{-\beta\hat{H}}$ for the Holstein Hamiltonian is expressed as a path integral by discretizing the imaginary time β into L_τ intervals and inserting complete sets of eigenstates of the quantum oscillator position operators. The trace over the electron degrees of freedom can be done analytically, and the trace over the phonon degrees of freedom is replaced by an integral over the oscillator eigenstates $x_{i,\tau}$, which now have both spatial (i) and imaginary time (τ) indices. The Boltzmann weight has a "bosonic" part, which couples $x_{i,\tau}$ locally, and so is rapid to evaluate, and a product of two fermion determinants [42]. Since the phonon field couples to the two spin species in the same way, the fermion determinants are identical. Hence the method has no "sign problem" [66–68].

Within DQMC, there are different methods with which the bosonic fields can be evolved. In the original formulation [64], individual updates at a single space-imaginary time point are proposed. The locality of this update makes the cost to evaluate the ratio of the new to old Boltzmann weights scale only as the square of the matrix dimension rather than its cube, as might be expected for a determinant evaluation. A full sweep of the lattice is then cubic in system size. We instead use a variant, "hybrid Monte Carlo," which updates all bosonic degrees of freedom simultaneously and is linear in the system size [69]. This method is especially effective for electron-phonon models, where the phonon kinetic energy moderates the variation of the field in imaginary time, and less effective in Hubbard models where such a term is absent [70].

An interesting feature of ML approaches and DQMC for the Holstein model, which we explore below, is the possibility of using different types of "snapshots" in the training. One can, for example, present the neural network with the space-imaginary time values of the phonon degrees of freedom $x_{i,\tau}$. Alternately, one can utilize the estimator of the density of electrons $1 - G(i,\tau)$. Here G is the inverse of the matrix the square of whose determinant is the fermionic contribution to the Boltzmann weight. A further flexibility is the ability to restrict to "equal-time" snapshots at a single τ, rather than snapshots over the entire space-imaginary time lattice. Finally, one can use correlation functions either of the phonon degrees of freedom $x_{i'\tau'}x_{i,\tau}$, or of the electrons $G(i',\tau')\,G(i,\tau)$.

C. Learning by confusion method

In a supervised binary classification problem, each training data sample is paired with a *correct* label, 0 or 1. Using a convolutional neural network (CNN), like the one used in our study and presented in Fig. 1(a), the task is to predict that correct label for as many test samples as possible. The LBC algorithm involves performing a sequence of supervised binary classification tasks, in which data samples are provided with modified (possibly *incorrect*) labels. In this approach, the classification task requires predicting the labels of the test sample, and the resulting accuracy is used to determine how

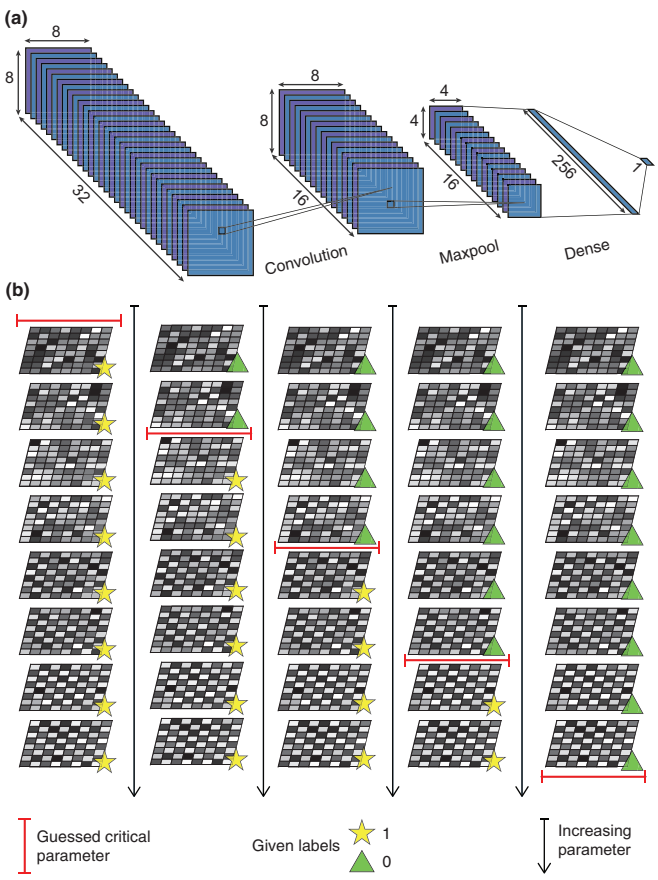

FIG. 1. (a) Architecture of the CNN used by the LBC technique. The input layer comprises a batch of 32 samples of size $L \times L$, shown here for $L = 8$. There are 16 kernels (filters) of size 3×3 applied on each data sample in the convolutional layer. The resulting data size is then cut by half after maxpooling. Finally, two dense layers, each with 256 nodes, connect to a single node to output a number between 0 and 1 (for simplicity, we show only one of these layers). (b) Schematics of LBC method. Eight different electron density snapshots are shown for increasing values of β from the top to the bottom. Here, a white pixel corresponds to 0 and a black pixel corresponds to 2. In every step, the LBC algorithm guesses a critical inverse-temperature β_c', marked as a red cursor. Data sets above and below β_c' are given different labels, marked as a yellow star and a green triangle for 1 and 0, respectively. The first and last steps of the algorithm are trivial: all the data sets have the same label and the accuracy to learn is perfect. In the middle column shown, the guessed labels match the actual labels of different phases, leading to a high accuracy on the middle peak of the $\mathcal{W}$ shape of the accuracy versus β plot. The second and fourth columns correspond to incorrect values $\beta_c' \neq \beta_c$ and hence lead to low accuracy.

close the labels are to the correct ones, and hence the location of the phase transition as a tuning parameter is varied. This process is illustrated in Fig. 1(b).

We illustrate how the LBC technique can be used to find the critical inverse temperature β_c in the square-lattice Holstein model, above which a long-range ordered CDW phase occurs. Our training and test data samples are obtained from the hybrid Monte Carlo simulations discussed in Sec. II B. These samples typically consist of $L \times L$ grids of local observables, such as the electron densities or phonon positions collected periodically during the measurement step of a simulation. Alternative data sets may include imaginary time-resolved density-density correlations.

Each DQMC simulation is performed for fixed values of β, λ_D, and ω_0, generating snapshots during the course of $N_{\text{meas}} = 10\,000$ sweeps of the space-imaginary time lattice. To determine β_c, we perform hybrid Monte Carlo simulations on N_p different values of $\beta_{\min} \leqslant \beta \leqslant \beta_{\max}$, keeping λ_D and ω_0 constant. Electron densities and phonon position snapshots are saved every n_s measurements, resulting in $N_{\text{snap}} = N_{\text{meas}}/n_s$ configurations for each β. The resulting data set has dimensions $(N_p \times N_{\text{snap}}, L \times L)$, where each row corresponds to a single snapshot. Density-density correlation datasets are built using snapshots from n_{it} equally spaced imaginary times and 100 different Monte Carlo times. The resulting dataset has dimension $(N_p \times n_{\text{it}} \times 100, L \times L)$. All snapshots are then reshaped into grayscale images and used as input for our CNN.

Every grayscale image is labeled based on its corresponding β. In a typical LBC run, a critical inverse temperature β_c' is chosen, and the input labels are modified accordingly: if $\beta \leqslant \beta_c'$, the image is assigned a label of 1, and if $\beta > \beta_c'$, it is assigned a label of 0. A binary classification task is then performed using these labels. Figure 1(b) illustrates five key scenarios in the LBC method. In the first and last cases, $\beta_c' = \beta_{\min}$ and $\beta_c' = \beta_{\max}$, respectively. Here, all input labels are identical, and the CNN is trained to label any test set in the same way, a task for which it easily achieves perfect performance.

More interesting scenarios arise when $\beta_{\min} < \beta_c' < \beta_{\max}$. If $\beta_c' = \beta_c$, the CNN performs optimally, as images with fundamentally different data patterns are assigned different labels *which correctly conform to the underlying physics* as contained in the snapshots. However, when $\beta_{\min} < \beta_c' < \beta_c$ or $\beta_c < \beta_c' < \beta_{\max}$, the CNN performs relatively poorly. In these cases, the data labels do not align well with the actual patterns. For example, if $\beta_c' > \beta_c$, many high-β data sets in the range $\beta_c < \beta < \beta_c'$ are incorrectly given low-β labels. This mismatch leads to the CNN becoming "confused," reflected in a failure to distinguish accurately between different data patterns.

The outcome of the five cases results in the characteristic $\mathcal{W}$-shaped curve of the LBC method, of which we will give examples in the next section (Figs. 3 and 6). The "outer" peaks of the $\mathcal{W}$ originate in the trivial, uniform label cases, $\beta_c' = \beta_{\min}$ and $\beta_c' = \beta_{\max}$. The inner peak of the $\mathcal{W}$ corresponds to the high accuracy of the CNN, which occurs when $\beta_c' = \beta_c$. This feature enables the LBC method to identify β_c within a range of β values by simply locating the middle peak of the $\mathcal{W}$. The LBC technique is especially useful in cases where obtaining an order parameter is challenging, or when an order parameter does not exist at all since only "raw" configurations of the degrees of freedom are employed. The LBC technique might also have additional advantages in bypassing the need for finite-size scaling analyses of correlation functions (which often have large error bars near the transition) to determine β_c. We will return to this issue in the conclusions.

The relative accuracy with which β_c can be determined certainly depends on N_p, the number of values between $\beta_{\min}$ and $\beta_{\max}$. We seek a value for N_p that ensures a critical parameter

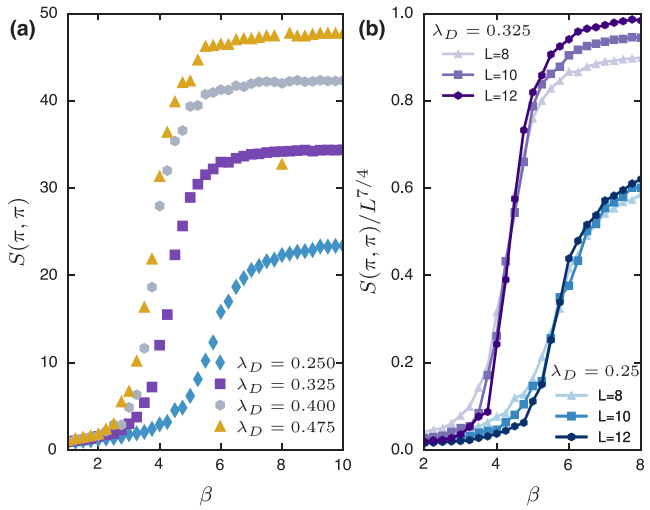

FIG. 2. (a) The CDW structure factor $S(\pi,\pi)$ for a β sweep plotted for four values of electron-phonon coupling $\lambda_D = 0.250, 0.325, 0.400, 0.475$. (b) The scaled CDW structure factor plotted for three lattice sizes and the first two values of λ_D. The rapid increase of $S(\pi,\pi)$, and the crossings, happen at values of β_c close to the location of the middle peak of the $\mathcal{W}$ shown in Fig. 6, i.e., in agreement with the LBC determinations of the critical points.

with reasonable accuracy and maintains a sufficient number of samples on both sides of the transition point. We also aim to avoid increasing N_p to the extent that training becomes inefficient. This parameter has been adjusted across different simulations, and we found that a value in the range of 25 to 50 is adequate for medium-sized intervals like those reported.

III. RESULTS

It is useful to put the results of LBC in the context of more "traditional" methods for locating the CDW transition. To this end we show, in Fig. 2, the CDW structure factor

$$S(\pi,\pi) \equiv \sum_j e^{i\pi(j_x+j_y)} \langle \hat{n}(j)\hat{n}(0)\rangle, \tag{2}$$

which sums the density-density correlation at separation $j = (j_x, j_y)$ with a phase appropriate to ordering of opposite sign on the two sublattices of the bipartite square lattice, versus β. At high temperatures, where the correlation function falls off rapidly with separation j, the structure factor is independent of lattice size. In the ordered phase, correlations extend across the entire lattice and $S(\pi,\pi) \propto L \times L$. These two regimes are evident in Fig. 2(a), with β_c roughly estimated as the place where $S(\pi,\pi)$ grows most rapidly. A more precise determination of β_c is obtained by scaling $S(\pi,\pi)$ using the known Ising universality class of the CDW transition, for which $\gamma/\nu = 7/4$. Curves for different L cross at β_c [Fig. 2(b)]. This is the procedure followed to determine β_c in most earlier DQMC studies of the Holstein model [37,41,45–48].

Figure 2(a) shows one underestimated value for $S(\pi,\pi)$ at $\beta = 8.00$ and $\lambda_D = 0.475$. This deviation occurs in a challenging strong-interaction and low-temperature regime. However, we note that several data points at even lower temperatures align with the expected trend. We conclude that this deviation does not undermine the validity of the results. We attribute this anomaly to insufficient statistical sampling performed at this point.

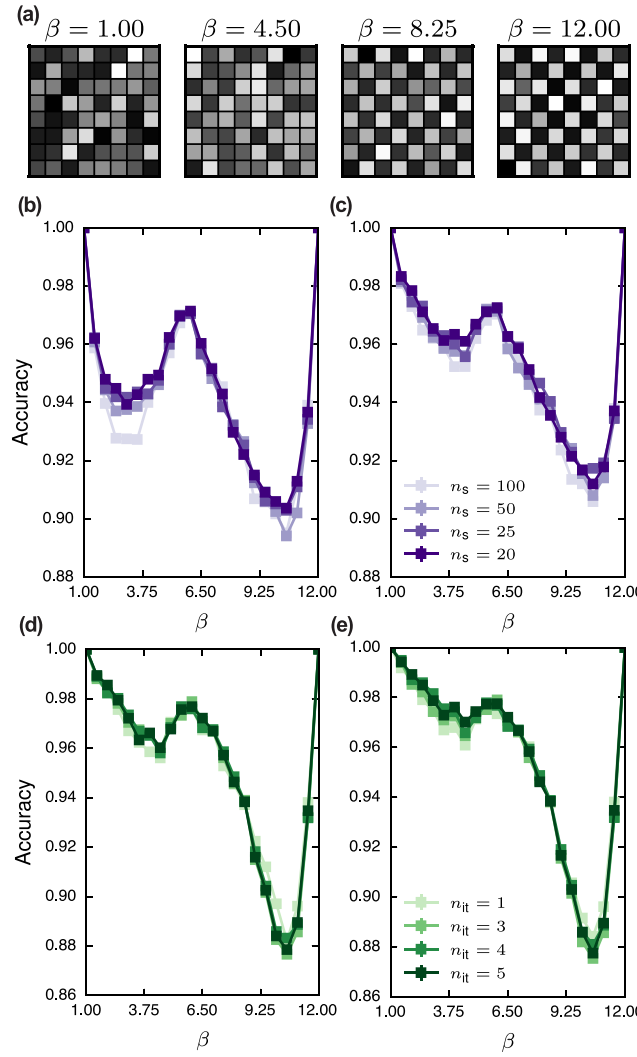

FIG. 3. Electron density snapshots taken at several temperatures are shown in (a); the emergence of a CDW pattern is clear at the two larger β. Also shown are LBC test accuracy for a sweep of (b) temperatures using electron density snapshots, (c) phonon positions snapshots, (d) density-density correlation data in real space, and (e) in momentum space. The four data types yield consistent positions for the interior maximum of the $\mathcal{W}$ at $\beta_c \sim 5.75$. Increasing the parameter n_s, the number of sweeps between snapshots, reduces the number of data sets used in the learning. However, increasing the parameter n_{it}, the number of different imaginary time slices used to build the density-density correlation datasets, increases it. The results for β_c are robust to changes in n_s, although the minima of the $\mathcal{W}$ deepen slightly as n_s grows. Here, $\lambda_D = 0.25$, $\omega_0 = 1.0$, and $L = 12$.

With that standard approach reviewed, we next present the results using LBC. We acquire snapshots from a family of simulations at different inverse-temperatures β using hybrid Monte Carlo simulations of the Holstein model on a square lattice of linear size $L = 12$ with $\omega_0 = 1.0$ and $\lambda = \sqrt{2}$ ($\lambda_D = 0.25$). The resulting snapshots are fed into the LBC CNN. We show results of the test accuracy for an

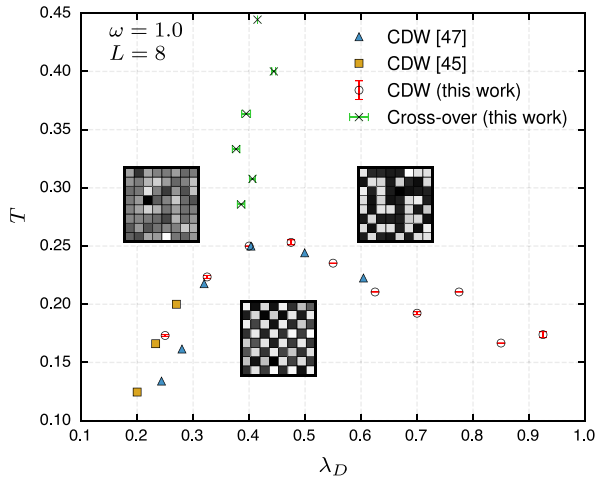

FIG. 4. The square lattice Holstein model T-λ_D phase diagram obtained with LBC for $L = 8$ and $\omega_0 = 1.0$. The red data points indicate the location of β_c shown in Fig. 6. Error bars are the standard error of the mean on ten different random seeds. Critical temperatures of the CDW transition in the range $0.250 \leqslant \lambda_D \lesssim 0.600$ show close agreement with previously obtained results [45,47]. The insets show a typical electron density snapshot taken in each of the three regions of the phase diagram. From left to right, snapshots are taken at $(\lambda_D, \beta) = (0.01, 3.50), (0.25, 12.00), (0.86, 3.50)$. The snapshots show the existence of three distinct phases: a disordered phase, a CDW phase, and a Fermi (bipolaron) liquid phase. The anomalous data point at $\lambda_D = 0.775$ is discussed in the text.

inverse-temperature sweep $a(\beta)$, using electron density snapshots, phonon position snapshots, and density-density correlation data in momentum and position space. Typical electron density snapshots at four different β values are shown in Fig. 3(a). By employing these distinct data types, the LBC results show a middle peak of the accuracy $a(\beta)$ for $\beta \sim 6$, agreeing with previously obtained results [41,45]. The $\mathcal{W}$ curves obtained from QMC data for the electron density [Fig. 3(b)] and phonon position [Fig. 3(c)] snapshots result in deeper accuracy minima at either side of the peak, which appear here at $\beta \approx 3$ and $\beta \approx 10$, compared to those observed in the density-density correlations or their Fourier transform, the structure factor [Figs. 3(d) and 3(e)].

Figure 3 further explores the dependence of the LBC results on the number of training electron density and phonon position data sets; $n_s = 20$ having five times the number of snapshots as $n_s = 100$. Although the shape of the $\mathcal{W}$ away from the interior maximum varies, we observe that the location of β_c is the same.

Next, we use the electronic density snapshots to perform similar LBC analyses at other values of λ_D, ranging from 0.250 to 0.925. The results are shown in Fig. 6 of the Appendix. The critical temperatures we obtain from them paint a complete picture of the CDW phase diagram of the half-filled Holstein model in the space of λ_D and temperature, which we show in Fig. 4. In that figure, circles with red error bars indicate the value of the critical temperature $T_c = 1/\beta_c$ for the transition from a disordered state at high temperatures, characterized by $S(\pi, \pi) \sim \mathcal{O}(1)$, to the CDW phase at low temperatures, exhibiting higher values of $S(\pi, \pi) \sim \mathcal{O}(L^2)$. We note that the critical temperatures obtained from the two sweeps in β at $\lambda_D = 0.250$ and $\lambda_D = 0.325$ agree with the ones extracted from the finite-size scaling analysis shown in Fig. 2. Additionally, Fig. 4 demonstrates the close alignment of the critical temperatures identified for the CDW transition in the range $0.250 \leqslant \lambda_D \lesssim 0.600$ with prior studies [45,47].

There is an anomalous data point in Fig. 4 at $\lambda_D = 0.775$ for which T_c is evidently overestimated. We include it to illustrate limitations of our current understanding of error estimation in the LBC method. Critical temperatures extracted from the structure factor, as in Fig. 2, can also sometimes lie substantially off the expected phase boundary. However, there are typically indications in the raw data, e.g., large error bars in the vicinity of the crossing, which signal the extracted data point might be unreliable. As can be seen in the $\lambda_D = 0.775$ panel of Fig. 6, the "warning sign" appears as a shoulder to the main middle peak in the shape of the $\mathcal{W}$, leading to a bump around $\beta = 5.8$, presumably marking the actual $T_c \sim 0.17$. Based on the trends we have seen in the λ_D sweeps (see Fig. 5 below), we attribute the unexpected extra peak in this diagram to finite-size effects.

It is natural to consider the effectiveness of LBC via a sweep in which λ_D is changed at fixed T. In a phase diagram of Fig. 4, this λ_D sweep is expected to first cross the phase boundary *horizontally* into a CDW phase at low-enough temperatures. The results of the LBC algorithm using electron density snapshots for λ_D sweeps at fixed β values are presented in Fig. 5. Typical snapshots across different λ_D's and at $\beta = 5.75$ (below the CDW dome) and $\beta = 3.50$ (above the CDW dome) are shown in Figs. 5(a) and 5(d), respectively. In Fig. 5(b) for $\beta = 5.75$ ($T = 0.174$), a clear $\mathcal{W}$ shape exhibits a middle peak that is located at $\lambda_{D_c} \approx 0.259$, in agreement with the results obtained from the β sweep performed at a fixed $\lambda_D = 0.250$, revealing a peak at $\beta_c \approx 5.75$ [see Figs. 3(b) and 6]. Figure 5(c) shows further consistent results at $\beta = 4.50$ ($T = 0.222$) for transitioning into the CDW phase at small λ_D.

The phase diagram of Fig. 4 emphasizes that at $T \gtrsim 0.250$, the CDW phase gives way to a disordered phase at all values of λ_D. However, the nature of this disordered phase at small λ_D ($\lesssim$0.4) is very different from that at large λ_D. In the former region, there is a mixture of empty, singly occupied, and doubly occupied sites, in which the entropy per site achieves its maximal value, $\ln 4$. However, for large values of λ_D ($\gtrsim$0.5), bipolarons are preferentially formed, and a gas of mostly empty and doubly occupied sites exists across the lattice, a regime where the entropy per site is $\ln 2$. Typical electron density snapshots shown at a relatively high temperature of $T = 0.286$ in Fig. 4 clearly display these behaviors. Their signature is also reflected in the value of the CDW structure factor in those regions. The latter is shown as a function of λ_D at $\beta = 5.75$ in Fig. 7 of the Appendix. While $S(\pi, \pi)$ is minimal around 1 in the completely disordered region of small λ_D, it saturates to a value around three times as much in the large-λ_D region.

The phonon snapshots of Fig. 5(d) show how the electron-phonon bond strengths evolve in this crossover. Note that the right-most panel of Fig. 5(d) [at $\lambda_D = 1.00$ and $\beta = 3.50$ ($T = 0.286$)] corresponds to empty and doubly occupied sites without the CDW pattern of the ordered phase [e.g.,

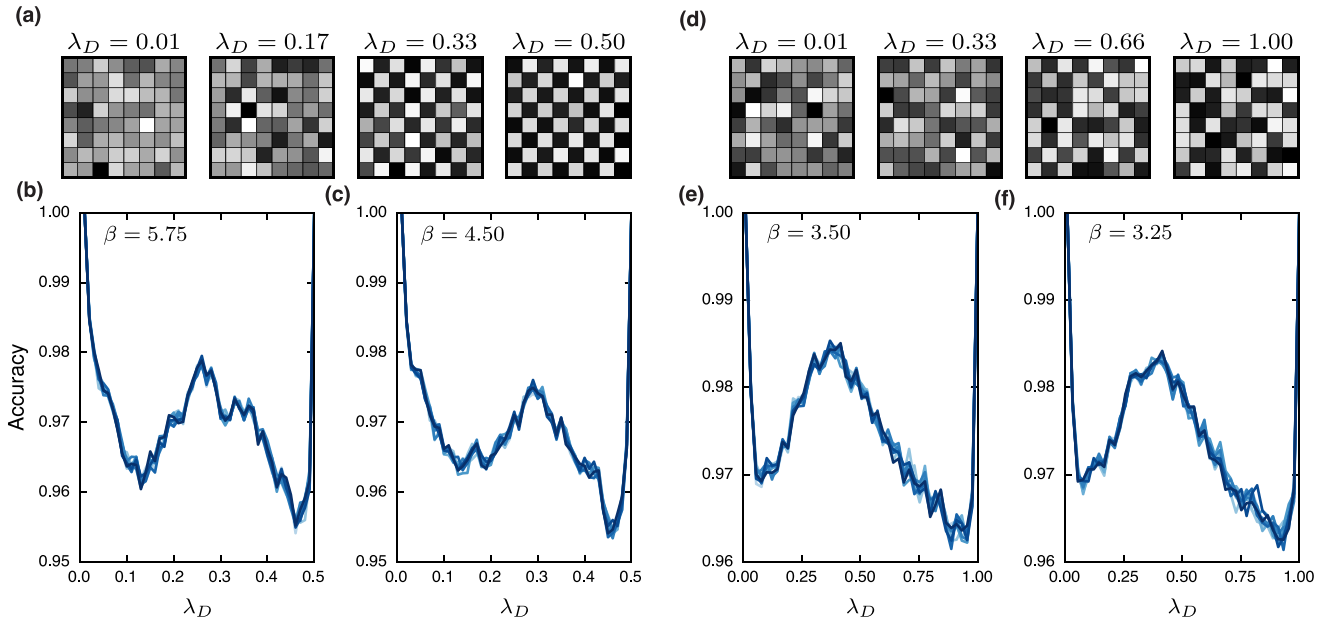

FIG. 5. Electron density snapshots taken at $\beta = 5.75$ are shown in (a), and the corresponding LBC test accuracy for a sweep of $N_p = 50$ values of λ_D using them is given in (b). A second sweep of λ_D at $\beta = 4.50$, also corresponding to a temperature *below* the CDW dome, is in (c). Here, the interior peaks of the $\mathcal{W}$ mark the onset of long range charge order. Phonon position snapshots taken at $\beta = 3.50$, shown in (d), reveal the emergence of long and short bonds without, however, an alternating pattern in their positions. The corresponding LBC test accuracies for a sweep of $N_p = 45$ values of λ_D using phonon position snapshots are shown at (e) $\beta = 3.50$ and (f) $\beta = 3.25$. Different lines correspond to ten different random number seeds. These temperatures are *above* the CDW dome, so the interior maximum of the $\mathcal{W}$ captures a cross-over to a gas of bipolarons. In electron density (phonon position) snapshots, white pixels correspond to 0 (-2) and black pixels correspond to 2 (2). All results are for $\omega_0 = 1.0$ and $L = 8$.

the latter is shown in the right-most panel in Fig. 3(a) at $\lambda_D = 0.25$ and $\beta = 12.00$ ($T \approx 0.083$)]. It is the *crossover* between the completely disordered and bipolaron regimes that is captured by our LBC analysis of λ_D sweeps at moderate temperatures above the CDW dome. Figures 5(e) and 5(f) show such sweeps for $\beta = 3.50$ ($T = 0.286$) and $\beta = 3.25$ ($T = 0.308$), respectively. We use phonon field snapshots for the LBC algorithm to obtain these results. The corresponding crossover temperatures are added to the phase diagram of Fig. 4 as crosses with green error bars. We find that using

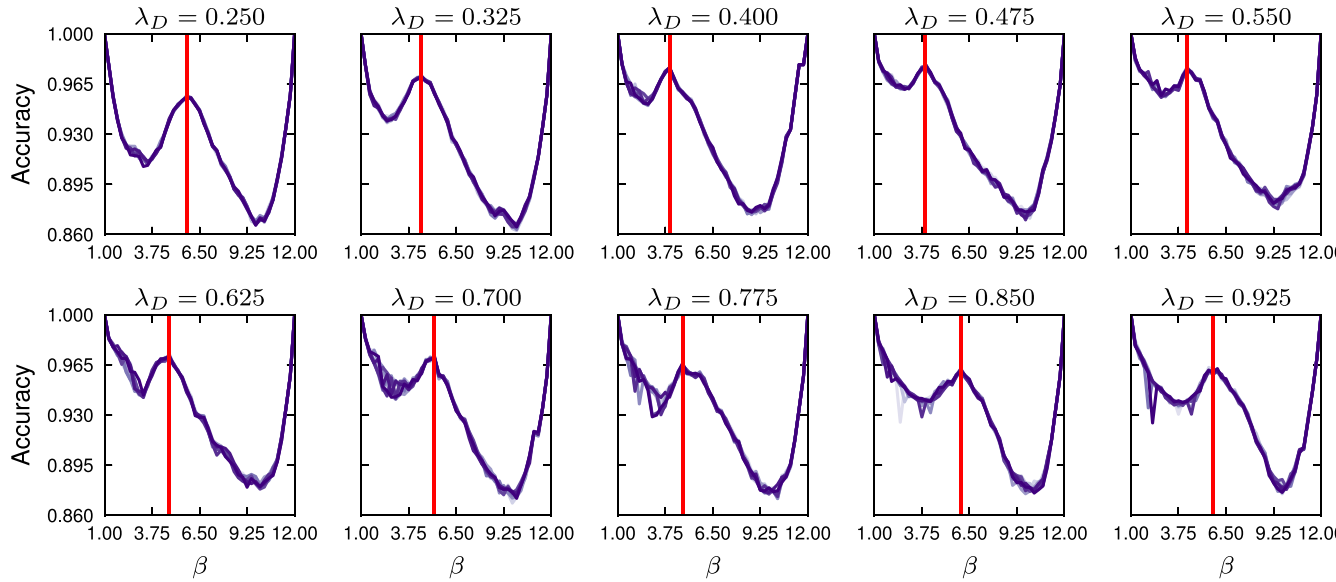

FIG. 6. The test accuracy of the LBC model for a sweep of β using electron density snapshots obtained for ten different values of λ_D. We take $\omega = 1.0$ and $n_s = 20$, and $N_p = 45$. The red vertical line is drawn at the location of the average middle peak of the $\mathcal{W}$, taken over the ten random number seeds shown.

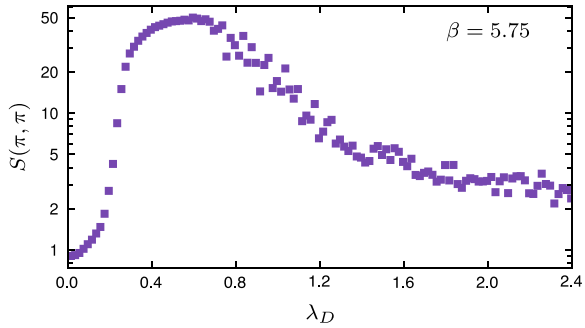

FIG. 7. The structure factor against λ_D at $\beta = 5.75$ plotted on a semi-log scale. $S(\pi,\pi)$ shows a visible difference between the completely disordered phase at low λ_D and the bipolaron structure at high λ_D.

electronic snapshots in this case leads to weaker results (see Fig. 8). Instead of a clear middle peak in the accuracy versus λ_D plots, we observe a shallow minimum in the small-λ_D region and a broad middle peak, followed by a relatively sharp minimum in the large-λ_D region.

The $\mathcal{W}$ curves for the λ sweeps of Fig. 5 are notably more noisy than the β sweeps of Figs. 3 and 6. We attribute this to our finite lattice size, and hence, the coarse resolution of the Brillouin zone. On a finite lattice and at low temperatures, the electron density exhibits a step-like structure as the chemical potential passes through the energies of the discrete k points. These fictitious jumps are removed by sufficiently strong interactions. However, our horizontal sweeps begin at rather small λ, where finite-size effects are large. We believe these then get reflected in the appearance of subsidiary structure in the $\mathcal{W}$. The smoother $\mathcal{W}$ curves of Figs. 3 and 6 all use larger λ_D, suppressing finite-size effects.

The crossover which is captured by the LBC method in Fig. 4 can be understood as follows: The half-filled repulsive Hubbard model is well known to exhibit two peaks in its specific heat as the temperature is lowered [71]. These correspond to, at higher temperature, the formation of local

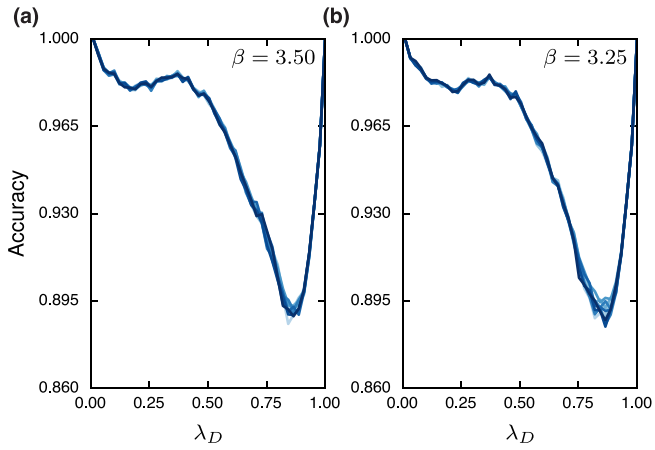

FIG. 8. The LBC test accuracy for a sweep of λ_D at (a) $\beta = 3.50$ and (b) $\beta = 3.25$ using electron density snapshots. Both temperatures lie *below* the CDW dome. Different lines correspond to ten different random number seeds.

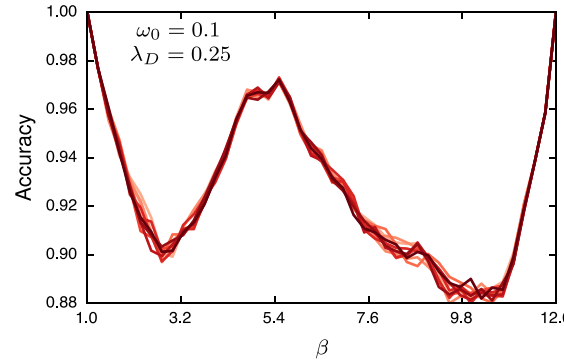

FIG. 9. The test accuracy of the LBC model for a sweep of β using electron density snapshots. Here, $\omega = 0.1$, $n_s = 100$, and $N_p = 45$. The success of LBC at this low value of ω_0 portrays the usefulness of LBC in the adiabatic limit $\omega_0 \to 0$.

moments (singly occupied sites) and the entropy loss as empty and doubly occupied sites are removed from the system, and at lower temperature to antiferromagnetic ordering of those moments. Indeed, a phase diagram similar to our Fig. 4 then results [4]. As a consequence of a well-known particle-hole transformation [72], the specific heat of the attractive Hubbard model has a similar structure, reflecting first the elimination of single occupied sites and then CDW formation as T decreases. It is also known that the Holstein model maps onto the attractive Hubbard model in the antiadiabatic limit $\omega_0 \to \infty$. In that sense, the phase diagram obtained from LBC is a plausible one. However, it has been shown that to achieve the limit in which Holstein quantitatively maps onto attractive Hubbard, $\omega_0/t \sim 100$ is required [73]. This is far from the $\omega_0/t = 1$ studied here. Thus, the observation of a crossover to a regime of randomly arranged empty and doubly occupied sites is a notable achievement of the LBC approach.

The LBC method also proves highly effective in the adiabatic regime of the Holstein model $\omega_0 \to 0$. In this limit, determining β_c is particularly challenging due to pronounced finite-size effects. Traditionally, finite-size scaling must be performed on relatively large lattice sizes to extract β_c with reasonable accuracy. To illustrate the usefulness of LBC in this limit, we perform a β sweep at fixed $\lambda_D = 0.250$ and $\omega = 0.1$. The accuracies, obtained from electron density snapshots, are shown in Fig. 9.

IV. DISCUSSION

In this paper we studied the CDW transition of the Holstein model, and the crossover to a gas of small polarons, with learning by confusion. One focus of our investigation was on the relative effectiveness of using spatial snapshots at a single imaginary time slice, versus using the full space-imaginary time lattice. In the case of the transverse field Ising model in d dimensions, the path-integral mapping of the partition function is to a classical Ising model in $d+1$ dimensions. In that case, withholding the imaginary time direction is precisely a matter of using snapshots only on a d-dimensional hyperplane embedded in a larger $d+1$-dimensional lattice. However, the simplicity of the transverse field Ising model mapping is atypical. In general, and here in the Holstein model

in particular, the space and imaginary time directions behave very differently. Hence, our results speak to the complex, and more generic situations when this is the case.

A commonly enunciated advantage of the LBC method is its ability to work directly with snapshots as opposed to requiring a structure factor or a particular (possibly unknown) order parameter. However, this is a property shared by a number of ML approaches [20]. Indeed, the principal component analysis also works directly with snapshots, with the additional feature that the leading eigenvector of the covariance matrix of data returns information about the order parameter [3]. While we have not done a careful study, our results suggest another possible advantage, namely, relatively small finite-size effects. Further work is needed to understand how the position of the inner peak of the $\mathcal{W}$, which encodes the critical point, depends on the lattice size, in analogy with techniques which have developed over the last few decades for the finite-size scaling of peaks in the specific heat and susceptibilities, as well as invariant quantities such as Binder ratios [74–76]. In the course of such a comparison, the question of whether LBC allows the determination of critical points with higher accuracy than "traditional" approaches (allowing for the analysis of both statistical and systematic error bars) can be better understood. Our current results suggest that LBC is a more efficient approach (using less CPU time) to obtaining the phase diagram of the Holstein Hamiltonian to the presented level of precision (a few percent uncertainty in β_c).

In this text, we portrayed the ability of LBC to detect both a real phase transition and a crossover. However, LBC does not retain specific underlying structures of the data that could be directly interpreted physically. Instead, at its highest level, LBC simply maps an input configuration to a label, namely, 0 or 1. Therefore, the current implementations of LBC do not distinguish between a real phase transition and a crossover in the same rigorous manner as the sophisticated finite-size scaling methods that have been developed. However, one viable approach to distinguish between a phase transition and a crossover with LBC is to examine how the critical temperature T_c, identified by the position of the interior peak in the $\mathcal{W}$, depends on linear lattice size: the functional form of the correction $T_c(L) = T_c(\infty) + AL^{-1/\nu}$ might then allow access to the critical exponent ν and the nature of the transition.

While density-density correlation data might be expected to yield the most accurate $\mathcal{W}$, our findings demonstrate that raw QMC data, such as electron densities and phonon positions, generally produce a clearer $\mathcal{W}$ with deeper minima. The choice between using electron densities or phonon positions depends on the specific parameters of the problem. For instance, electron density snapshots yielded a clearer $\mathcal{W}$ when sweeping β to explore the CDW transition, whereas phonon position snapshots proved more effective for analyzing the crossover during a λ_D sweep. The ability of the LBC method and other ML approaches to only require snapshots already eliminates the need of considering to feed correlation snapshots into the model. This is promising since to an extent, extracting the location of a phase transition from correlation data is not too far from giving the machine the answer we expect from it.

We conclude by noting a subtle feature of the LBC method. It is evident in the results presented in this work that the minima in the $\mathcal{W}$ curve can typically be not so much reduced from unity; in several of our plots the *lowest* accuracy is as high as 0.93, despite the fact that those β values correspond to the data sets being the "most mislabeled," i.e., β_c' very far from the correct β_c. The explanation reflects the power of ML and training. Given enough time (epochs) and fitting parameters (weights and biases), a CNN should ultimately be able to learn to classify test sets according even to "incorrect" labels. Thus in some sense the minima in the $\mathcal{W}$ curves are reliant on the limitation of resources [52].

ACKNOWLEDGMENT

This work was supported by Grant No. DE-SC0022311 funded by the U.S. Department of Energy, Office of Science.

DATA AVAILABILITY

The data that support the findings of this article are openly available [77], embargo periods may apply.

APPENDIX: ADDITIONAL SUPPORTING PLOTS

We repeat the same β sweep in the main text for ten different values of λ_D and show the results in Fig. 6. Here we use a lattice size $L = 8$. Indeed, we see very little variation of the $\mathcal{W}$ curves with lattice size (compare, for example, Fig. 3 with the top left panel of Fig. 6, which shows results for the same $\lambda_D = 0.25$.) The red vertical lines in Fig. 6 represent the location of β_c for the ten different values of λ_D.

In Fig. 7, we show the CDW structure factor as a function of λ_D at $\beta = 5.75$ in a semi-log plot. It shows that $S(\pi, \pi)$ is larger, by a about a factor of 3, in the large-λ_D region, where the system is expected to consist of mostly a gas of empty and doubly occupied sites, in comparison to the completely disordered small-λ_D region before the peak.

In Fig. 8, we show the same plots as in Figs. 5(e) and 5(f) of the main text, except that electronic snapshots, as opposed to phonon position snapshots, are used. In this case, we find a broader peak and a shallower minimum in the small-λ_D region.

[1] L. Wang, Discovering phase transitions with unsupervised learning, Phys. Rev. B **94**, 195105 (2016).

[2] J. Carrasquilla and R. G. Melko, Machine learning phases of matter, Nat. Phys. **13**, 431 (2017).

[3] W. Hu, R. R. P. Singh, and R. T. Scalettar, Discovering phases, phase transitions, and crossovers through unsupervised machine learning: A critical examination, Phys. Rev. E **95**, 062122 (2017).

[4] K. Ch'Ng, J. Carrasquilla, R. G. Melko, and E. Khatami, Machine learning phases of strongly correlated fermions, Phys. Rev. X **7**, 031038 (2017).

[5] G. Carleo and M. Troyer, Solving the quantum many-body problem with artificial neural networks, Science **355**, 602 (2017).

[6] Y. Zhang and E.-A. Kim, Quantum loop topography for machine learning, Phys. Rev. Lett. **118**, 216401 (2017).

[7] K. Ch'ng, N. Vazquez, and E. Khatami, Unsupervised machine learning account of magnetic transitions in the Hubbard model, Phys. Rev. E **97**, 013306 (2018).

[8] S. J. Wetzel, Unsupervised learning of phase transitions: From principal component analysis to variational autoencoders, Phys. Rev. E **96**, 022140 (2017).

[9] P. Huembeli, A. Dauphin, and P. Wittek, Identifying quantum phase transitions with adversarial neural networks, Phys. Rev. B **97**, 134109 (2018).

[10] J. Venderley, V. Khemani, and E.-A. Kim, Machine learning out-of-equilibrium phases of matter, Phys. Rev. Lett. **120**, 257204 (2018).

[11] A. Bohrdt, S. Kim, A. Lukin, M. Rispoli, R. Schittko, M. Knap, M. Greiner, and J. Léonard, Analyzing nonequilibrium quantum states through snapshots with artificial neural networks, Phys. Rev. Lett. **127**, 150504 (2021).

[12] S. Zhang, P. Zhang, and G.-W. Chern, Anomalous phase separation in a correlated electron system: Machine-learning–enabled large-scale kinetic Monte Carlo simulations, Proc. Natl. Acad. Sci. USA **119**, e2119957119 (2022).

[13] M. Rodriguez-Vega, M. G. Vergniory, and G. A. Fiete, Quantum materials out of equilibrium, Phys. Today **75**, 42 (2022).

[14] A. Bohrdt, C. S. Chiu, G. Ji, M. Xu, D. Greif, M. Greiner, E. Demler, F. Grusdt, and M. Knap, Classifying snapshots of the doped Hubbard model with machine learning, Nat. Phys. **15**, 921 (2019).

[15] B. S. Rem, N. Käming, M. Tarnowski, L. Asteria, N. Fläschner, C. Becker, K. Sengstock, and C. Weitenberg, Identifying quantum phase transitions using artificial neural networks on experimental data, Nat. Phys. **15**, 917 (2019).

[16] Y. Zhang, A. Mesaros, K. Fujita, S. D. Edkins, M. H. Hamidian, K. Ch'ng, H. Eisaki, S. Uchida, J. C. S. Davis, E. Khatami *et al.*, Machine learning in electronic-quantum-matter imaging experiments, Nature (London) **570**, 484 (2019).

[17] G. Torlai, B. Timar, E. P. L. van Nieuwenburg, H. Levine, A. Omran, A. Keesling, H. Bernien, M. Greiner, V. Vuletić, M. D. Lukin, R. G. Melko, and M. Endres, Integrating neural networks with a quantum simulator for state reconstruction, Phys. Rev. Lett. **123**, 230504 (2019).

[18] E. Khatami, E. Guardado-Sanchez, B. M. Spar, J. F. Carrasquilla, W. S. Bakr, and R. T. Scalettar, Visualizing strange metallic correlations in the two-dimensional Fermi-Hubbard model with artificial intelligence, Phys. Rev. A **102**, 033326 (2020).

[19] A. M. Samarakoon, K. Barros, Y. W. Li, M. Eisenbach, Q. Zhang, F. Ye, V. Sharma, Z. L. Dun, H. Zhou, S. A. Grigera *et al.*, Machine-learning-assisted insight into spin ice $Dy_2Ti_2O_7$, Nat. Commun. **11**, 892 (2020).

[20] S. Johnston, E. Khatami, and R. Scalettar, A perspective on machine learning and data science for strongly correlated electron problems, Carbon Trends **9**, 100231 (2022).

[21] A. Dawid, J. Arnold, B. Requena, A. Gresch, M. Płodzień, K. Donatella, K. A. Nicoli, P. Stornati, R. Koch, M. Büttner *et al.*, Modern applications of machine learning in quantum sciences, arXiv:2204.04198.

[22] J. Carrasquilla, Machine learning for quantum matter, Adv. Phys.: X **5**, 1797528 (2020).

[23] Y. Nomura, A. S. Darmawan, Y. Yamaji, and M. Imada, Restricted Boltzmann machine learning for solving strongly correlated quantum systems, Phys. Rev. B **96**, 205152 (2017).

[24] P. Broecker, F. F. Assaad, and S. Trebst, Quantum phase recognition via unsupervised machine learning, arXiv:1707.00663.

[25] K. Shinjo, K. Sasaki, S. Hase, S. Sota, S. Ejima, S. Yunoki, and T. Tohyama, Machine learning phase diagram in the half-filled one-dimensional extended Hubbard model, J. Phys. Soc. Jpn. **88**, 065001 (2019).

[26] A. Canabarro, F. F. Fanchini, A. L. Malvezzi, R. Pereira, and R. Chaves, Unveiling phase transitions with machine learning, Phys. Rev. B **100**, 045129 (2019).

[27] S. Striegel, E. Ibarra-García-Padilla, and E. Khatami, Machine learning detection of correlations in snapshots of ultracold atoms in optical lattices, arXiv:2310.03267.

[28] B. Xiao, J. R. Moreno, M. Fishman, D. Sels, E. Khatami, and R. Scalettar, Extracting off-diagonal order from diagonal basis measurements, Phys. Rev. Res. **6**, L022064 (2024).

[29] C. Chen, X. Y. Xu, J. Liu, G. Batrouni, R. Scalettar, and Z. Y. Meng, Symmetry-enforced self-learning Monte Carlo method applied to the Holstein model, Phys. Rev. B **98**, 041102(R) (2018).

[30] S. Li, P. M. Dee, E. Khatami, and S. Johnston, Accelerating lattice quantum Monte Carlo simulations using artificial neural networks: Application to the Holstein model, Phys. Rev. B **100**, 020302(R) (2019).

[31] Y. Nomura, Machine learning quantum states—extensions to fermion–boson coupled systems and excited-state calculations, J. Phys. Soc. Jpn. **89**, 054706 (2020).

[32] C. Cheng, S. Zhang, and G.-W. Chern, Machine learning for phase ordering dynamics of charge density waves, Phys. Rev. B **108**, 014301 (2023).

[33] Th. Holstein, Studies of polaron motion: Part I. The molecular-crystal model, Ann. Phys. **8**, 325 (1959).

[34] R. E. Peierls, *Surprises in Theoretical Physics* (Princeton University Press, Princeton, 1979), Vol. 107.

[35] J. E. Hirsch and E. Fradkin, Effect of quantum fluctuations on the Peierls instability: A Monte Carlo study, Phys. Rev. Lett. **49**, 402 (1982).

[36] J. E. Hirsch and E. Fradkin, Phase diagram of one-dimensional electron-phonon systems. II. The molecular-crystal model, Phys. Rev. B **27**, 4302 (1983).

[37] R. T. Scalettar, N. E. Bickers, and D. J. Scalapino, Competition of pairing and Peierls–charge-density-wave correlations in a two-dimensional electron-phonon model, Phys. Rev. B **40**, 197 (1989).

[38] F. Marsiglio, Pairing and charge-density-wave correlations in the Holstein model at half-filling, Phys. Rev. B **42**, 2416 (1990).

[39] J. K. Freericks, M. Jarrell, and D. J. Scalapino, Holstein model in infinite dimensions, Phys. Rev. B **48**, 6302 (1993).

[40] T. Ohgoe and M. Imada, Competition among superconducting, antiferromagnetic, and charge orders with intervention by phase separation in the 2D Holstein-Hubbard model, Phys. Rev. Lett. **119**, 197001 (2017).

[41] M. Hohenadler and G. G. Batrouni, Dominant charge density wave correlations in the Holstein model on the half-filled square lattice, Phys. Rev. B **100**, 165114 (2019).

[42] O. Bradley, G. G. Batrouni, and R. T. Scalettar, Superconductivity and charge density wave order in the two-dimensional Holstein model, Phys. Rev. B **103**, 235104 (2021).

[43] B. Nosarzewski, E. W. Huang, P. M. Dee, I. Esterlis, B. Moritz, S. A. Kivelson, S. Johnston, and T. P. Devereaux, Superconductivity, charge density waves, and bipolarons in the Holstein model, Phys. Rev. B **103**, 235156 (2021).

[44] M. V. Araújo, J. P. de Lima, S. Sorella, and N. C. Costa, Two-dimensional $t - t'$ Holstein model, Phys. Rev. B **105**, 165103 (2022).

[45] M. Weber and M. Hohenadler, Two-dimensional Holstein-Hubbard model: Critical temperature, Ising universality, and bipolaron liquid, Phys. Rev. B **98**, 085405 (2018).

[46] Y.-X. Zhang, W.-T. Chiu, N. C. Costa, G. G. Batrouni, and R. T. Scalettar, Charge order in the Holstein model on a honeycomb lattice, Phys. Rev. Lett. **122**, 077602 (2019).

[47] C. Feng and R. T. Scalettar, Interplay of flat electronic bands with Holstein phonons, Phys. Rev. B **102**, 235152 (2020).

[48] C. Chen, X. Y. Xu, Z. Y. Meng, and M. Hohenadler, Charge-density-wave transitions of Dirac fermions coupled to phonons, Phys. Rev. Lett. **122**, 077601 (2019).

[49] I. Esterlis, S. A. Kivelson, and D. J. Scalapino, A bound on the superconducting transition temperature, npj Quantum Mater. **3**, 59 (2018).

[50] E. P. L. Van Nieuwenburg, Y.-H. Liu, and S. D. Huber, Learning phase transitions by confusion, Nat. Phys. **13**, 435 (2017).

[51] J. Arnold, F. Schäfer, and N. Lörch, Fast detection of phase transitions with multi-task learning-by-confusion, arXiv:2311.09128.

[52] S. S. Lee and B. J. Kim, Confusion scheme in machine learning detects double phase transitions and quasi-long-range order, Phys. Rev. E **99**, 043308 (2019).

[53] M. J. S. Beach, A. Golubeva, and R. G. Melko, Machine learning vortices at the Kosterlitz-Thouless transition, Phys. Rev. B **97**, 045207 (2018).

[54] M. Richter-Laskowska, M. Kurpas, and M. M. Maśka, Learning by confusion approach to identification of discontinuous phase transitions, Phys. Rev. E **108**, 024113 (2023).

[55] M. A. Gavreev, A. S. Mastiukova, E. O. Kiktenko, and A. K. Fedorov, Learning entanglement breakdown as a phase transition by confusion, New J. Phys. **24**, 073045 (2022).

[56] D. Zvyagintseva, H. Sigurdsson, V. K. Kozin, I. Iorsh, I. A. Shelykh, V. Ulyantsev, and O. Kyriienko, Machine learning of phase transitions in nonlinear polariton lattices, Commun. Phys. **5**, 8 (2022).

[57] Y. A. Kharkov, V. E. Sotskov, A. A. Karazeev, E. O. Kiktenko, and A. K. Fedorov, Revealing quantum chaos with machine learning, Phys. Rev. B **101**, 064406 (2020).

[58] E. Greplova, A. Valenti, G. Boschung, F. Schäfer, N. Lörch, and S. D. Huber, Unsupervised identification of topological phase transitions using predictive models, New J. Phys. **22**, 045003 (2020).

[59] C. Franchini, M. Reticcioli, M. Setvin, and U. Diebold, Polarons in materials, Nat. Rev. Mater. **6**, 560 (2021).

[60] N. V. Prokof'ev and B. V. Svistunov, Polaron problem by diagrammatic quantum Monte Carlo, Phys. Rev. Lett. **81**, 2514 (1998).

[61] B. J. Powell, An introduction to effective low-energy Hamiltonians in condensed matter physics and chemistry, arXiv:0906.1640.

[62] B. Cohen-Stead, K. Barros, Z. Y. Meng, C. Chen, R. T. Scalettar, and G. G. Batrouni, Langevin simulations of the half-filled cubic Holstein model, Phys. Rev. B **102**, 161108(R) (2020).

[63] P. M. Dee, K. Nakatsukasa, Y. Wang, and S. Johnston, Temperature-filling phase diagram of the two-dimensional holstein model in the thermodynamic limit by self-consistent migdal approximation, Phys. Rev. B **99**, 024514 (2019).

[64] R. Blankenbecler, D. J. Scalapino, and R. L. Sugar, Monte Carlo calculations of coupled boson-fermion systems. I, Phys. Rev. D **24**, 2278 (1981).

[65] S. R. White, D. J. Scalapino, R. L. Sugar, E. Y. Loh, J. E. Gubernatis, and R. T. Scalettar, Numerical study of the two-dimensional Hubbard model, Phys. Rev. B **40**, 506 (1989).

[66] E. Y. Loh, J. E. Gubernatis, R. T. Scalettar, S. R. White, D. J. Scalapino, and R. L. Sugar, Sign problem in the numerical simulation of many-electron systems, Phys. Rev. B **41**, 9301 (1990).

[67] V. I. Iglovikov, E. Khatami, and R. T. Scalettar, Geometry dependence of the sign problem in quantum Monte Carlo simulations, Phys. Rev. B **92**, 045110 (2015).

[68] R. Mondaini, S. Tarat, and R. T. Scalettar, Quantum critical points and the sign problem, Science **375**, 418 (2022).

[69] B. Cohen-Stead, O. Bradley, C. Miles, G. Batrouni, R. Scalettar, and K. Barros, Fast and scalable quantum Monte Carlo simulations of electron-phonon models, Phys. Rev. E **105**, 065302 (2022).

[70] R. T. Scalettar, D. J. Scalapino, R. L. Sugar, and D. Toussaint, Hybrid molecular-dynamics algorithm for the numerical simulation of many-electron systems, Phys. Rev. B **36**, 8632 (1987).

[71] T. Paiva, R. T. Scalettar, C. Huscroft, and A. K. McMahan, Signatures of spin and charge energy scales in the local moment and specific heat of the half-filled two-dimensional Hubbard model, Phys. Rev. B **63**, 125116 (2001).

[72] R. R. P. Singh and R. T. Scalettar, Exact demonstration of η pairing in the ground state of an attractive-U Hubbard model, Phys. Rev. Lett. **66**, 3203 (1991).

[73] C. Feng, H. Guo, and R. T. Scalettar, Charge density waves on a half-filled decorated honeycomb lattice, Phys. Rev. B **101**, 205103 (2020).

[74] K. Binder, Finite size scaling analysis of ising model block distribution functions, Z. Phys. B **43**, 119 (1981).

[75] K. Binder and D. P. Landau, Finite-size scaling at first-order phase transitions, Phys. Rev. B **30**, 1477 (1984).

[76] A. W. Sandvik, Finite-size scaling of the ground-state parameters of the two-dimensional Heisenberg model, Phys. Rev. B **56**, 11678 (1997).

[77] Available in our data repository at https://ucdavis.app.box.com/folder/304696521244.